
PERGAMON

Journal of Quantitative Spectroscopy & Radiative Transfer 83 (2004) 63–81

Journal of Quantitative Spectroscopy & Radiative Transfer

www.elsevier.com/locate/jqsrt

Temperature dependent pressure induced lineshape of O_3 rotational transitions in air

Brian J. Drouin[a,*], Jonathan Fischer[b], Robert R. Gamache[b]

[a] *Jet Propulsion Laboratory, California Institute of Technology, Pasadena, CA 91109-8099, USA*
[b] *Department of Environmental, Earth, and Atmospheric Sciences, University of Massachusetts Lowell, 1 University Avenue, Lowell, MA 01854, USA*

Received 15 July 2002; accepted 16 October 2002

Abstract

The pressure induced broadening of a series of pure rotational transitions of ozone have been measured as a function of temperature. Results of experiments are compared with calculations employing the complex semiclassical theory of Robert and Bonamy. This set of rotational transitions is the dominant feature of the millimeter and submillimeter ozone spectra to be measured in the upcoming EOS-MLS mission.

PACS: 33.70.Jg; 33.70.−w; 34.10.+x; 05.10.−a; 33.20.−t; 33.20.Bx; 07.57.−c

Keywords: Ozone; Linewidths; Pressure broadening; Atmospheric Spectra; Lineshape

1. Introduction

Increased monitoring and improved modeling of ozone in the terrestrial atmosphere has continued to push the state-of-the-art for ozone spectroscopy. Many missions involving satellite, balloon, aircraft and ground-based measurements have produced valuable data sets regarding ozone concentrations, in both columns and profiles. Methods utilizing emissive remote sensing have proven to be extremely valuable due to the broad range of spatial and temporal coverage available [1–5]. The earth observing system—microwave limb sounder (EOS-MLS) instrument [1], part of NASA's AURA spacecraft, will take advantage of these factors by continuously monitoring ozone profiles through limb-sounding measurements in a sun-synchronous orbit. Since ozone radiates energy through the rotational band at the temperatures found in the troposphere and stratosphere, observation of these discrete air broadened signals in the 240 and 640 GHz radiometers will directly identify the concentration of ozone along

* Corresponding author. Fax: +1-818-354-8460.
E-mail address: bdrouin@mail2.jpl.nasa.gov (B.J. Drouin).

0022-4073/04/$ - see front matter
PII: S0022-4073(02)00293-5

the line of sight. Designed improvements in sensitivity, efficiency and frequency coverage compared to the UARS-MLS (in operation since 1991) will allow unprecedented signal-to-noise ratios for the strongest transitions found in these bands.

For processing of the radiative signatures into meaningful concentration profiles it is imperative that accurate and precise spectroscopic parameters be used to analyze the observed lineshapes. Rotational transition frequencies, as well as intensities, are known to sufficient accuracy and precision as catalogued in the JPL millimeter and submillimeter spectral line database [6] and in HITRAN [7]. These parameters are well understood quantum mechanically, and where not directly measured, can be interpolated. However, radiative molecules in perturbed environments (such as the terrestrial atmosphere) experience broadening and/or shifting of the natural lineshape. Such effects are typically directly proportional to the number of perturbing species (pressure) and inversely proportional to the logarithm of the temperature. Furthermore, a decrease in collisional cross-section is generally observed at elevated rotational quanta. Currently, the state-of-the-art semi-classical treatment [8] that describes these foreign gas perturbations can reproduce these trends, furthermore, and recent progress [9] has improved the accuracy to a few percent. However, recent and future missions require accuracies for pressure broadening parameters to better than a few percent. Nonetheless, the theory confirms the functional form of the pressure and temperature dependencies within the atmospheric temperature range, and thus insures the reliability of the empirical use of this model. Theory has been developed alongside the abundance of rotationally resolved *vibrational* spectra, for which a much greater amount of data is available in comparison to the rotational band. Comparisons of infrared and pure rotational lineshape parameters are quite favorable for this species [10], in agreement with the results of theoretical predictions.

In this paper new measurements of pure rotational transition lineshapes of a series of transitions in the EOS-MLS bands is reported as well as new semi-classical calculations of the same parameters. In depth comparisons to existing rotational and vibrational (v_1 band only) data, will be made for similar type transitions.

2. Experimental details

Measurements were carried out with the submillimeter radiation passed twice through a 0.5 m length, 7.3 cm diameter, temperature controlled glass cell. The entire experimental design is shown in Fig. 1. A liquid-helium cooled InSb bolometer was used for detection of the frequency modulated source. The mm and submm sources consisted of a Hewlett Packard phase-locked sweep synthesizer operating at ~ 12 GHz followed by an active sextupler (Millitech or Agilent) that pumps either a Custom-Microwave whisker contacted diode, a n-harmonic generator (x2, x3), or a JPL-built antiparallel planar Schottky diode odd-harmonic multiplier (x7) [11]. The implementation of this multiplier chain (opposed to a phase-locked mm-wave source) provides an easily tunable, stable, synthesized radiation source for performing spectroscopy and linewidth measurements.

Table 1 lists the frequencies and quanta of the measured transitions. A simulation of the mm-wave transitions in the 230–252 GHz range is shown in Fig. 2. Spectral lineshapes were measured over a 16–20 MHz interval about each line center as the pressure and temperature were systematically adjusted. Modulation depths of 2–4 MHz were sufficient for producing high signal-to-noise (S/N) second derivative spectra. The modulation depth is chosen for optimal S/N at higher pressures, therefore

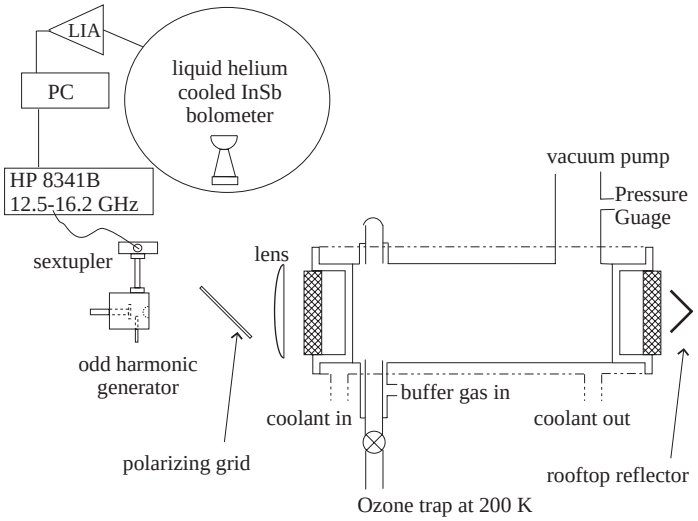

Fig. 1. Experimental setup for measurement of O_3 linewidths.

Table 1
Ozone transitions examined in this study

$J'_{K'_aK'_c}$	$J_{K_aK_c}$	ν (MHz)	$\log(I_{ba})$
$5_{1,5}$	$4_{0,4}$	208642.44	−4.17[a]
$7_{1,7}$	$6_{0,6}$	249788.60	−3.90
$8_{3,5}$	$9_{2,8}$	244158.04	−4.55
$9_{1,9}$	$8_{0,8}$	288959.14	−3.68[a]
$10_{2,8}$	$10_{1,9}$	249961.96	−3.76
$12_{0,12}$	$11_{1,11}$	243453.70	−3.76
$12_{2,10}$	$12_{1,11}$	242318.74	−3.72
$14_{1,13}$	$14_{0,14}$	195430.51	−3.92[a]
$14_{2,12}$	$14_{1,13}$	237146.19	−3.69
$16_{1,15}$	$16_{0,16}$	231281.49	−3.83
$16_{2,14}$	$16_{1,15}$	235709.84	−3.67
$15_{4,12}$	$16_{3,13}$	247761.77	−4.42
$15_{6,10}$	$16_{5,11}$	625371.47	−3.87
$18_{1,17}$	$18_{0,18}$	273050.90	−3.76
$18_{2,16}$	$18_{1,17}$	239093.26	−3.66
$20_{2,18}$	$20_{1,19}$	248183.38	−3.66
$25_{1,25}$	$24_{0,24}$	610365.33	−2.92
$24_{5,19}$	$25_{4,22}$	206132.05	−4.72[b]
$28_{1,27}$	$28_{0,28}$	535922.77	−3.62[a]
$30_{1,29}$	$30_{0,30}$	591249.01	−3.64
$31_{10,22}$	$30_{9,21}$	2543208.40	−2.76[a]
$37_{9,29}$	$36_{8,28}$	2509560.44	−3.00[a]

[a]These transitions are calculated only in this study.
[b]This transition was previously measured in Ref. [13].

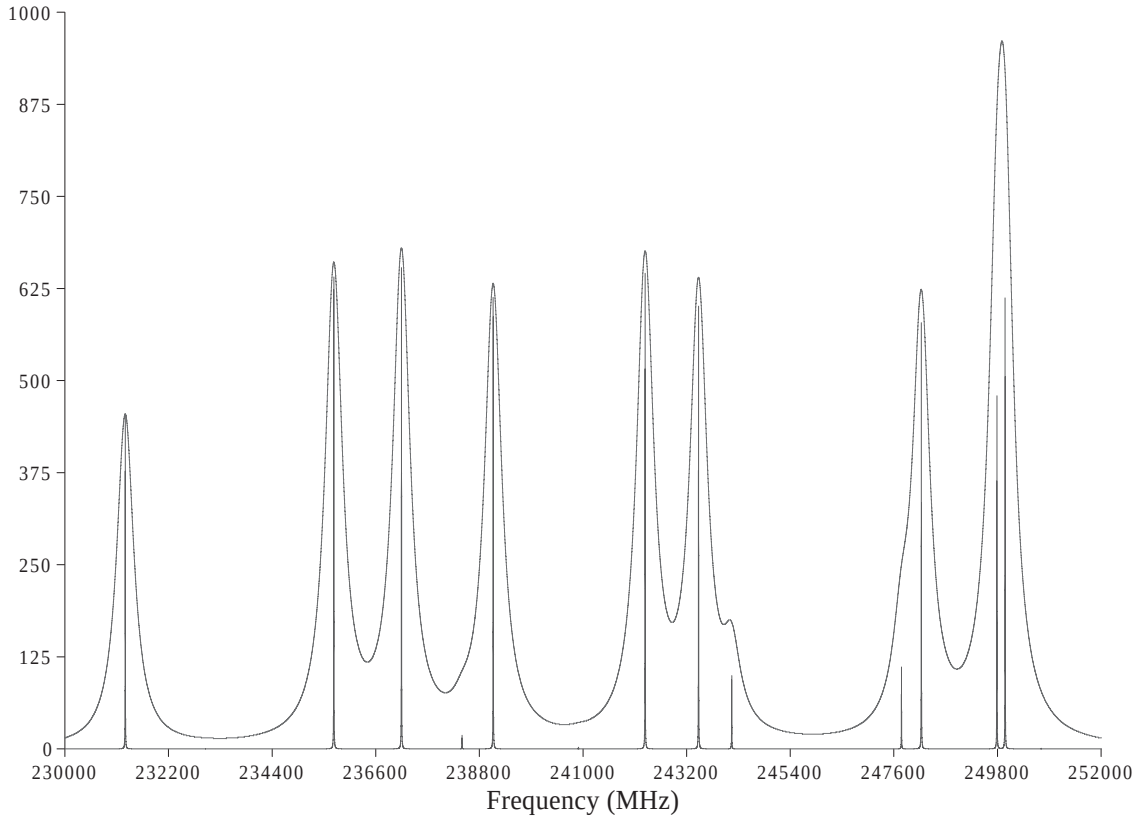

Fig. 2. Simulation of O_3 rotational transitions in the 230–252 GHz region, all half-widths are 2.9 MHz/Torr, traces are depicted for 1.3 (thin spikes) and 133 Torr (partially resolved) of air.

resulting in over-modulated low pressure spectra. See Fig. 3 for typical baseline-subtracted sweeps at various pressures during a fixed-temperature run. At low pressure, the linewidth is dominated by the modulation and the influence of pressure broadening on the instrumental lineshape is observed only in the increased spacing between the side-lobes of the second derivative spectra. Each scan is preceded and followed by a scan of the cell with no absorber present for a reliable baseline subtraction. For application of the convolution method [12] to the spectra it is imperative that all reference and test spectra are completely enclosed within the given scan range.

Ozone is produced in modest amounts through cryogenic trapping of the output of an ozonizer on silica gel immersed in a dry ice/ethanol bath at 190 K. Initial pumping on the trap reduces the O_2 partial pressure to a minimum prior to flowing the O_3 through the spectrometer.

The spectrometer cell is temperature controlled by flowing $N_{2(l)}$ cooled methanol through a sleeve surrounding the cell. The gases flowing through the cell rapidly thermally equilibrate. Maximum flow speeds of $\sim$24 l/s were found to give more consistent results; no pressure gradient was observed across the flow cell. The temperature is monitored using a pair of 'T' type thermocouples, one imbedded in the coolant sleeve and the other resting in an ice bath. The coolant temperature can be regulated to within 2° of the desired temperature down to 190 K. The teflon windows are inset

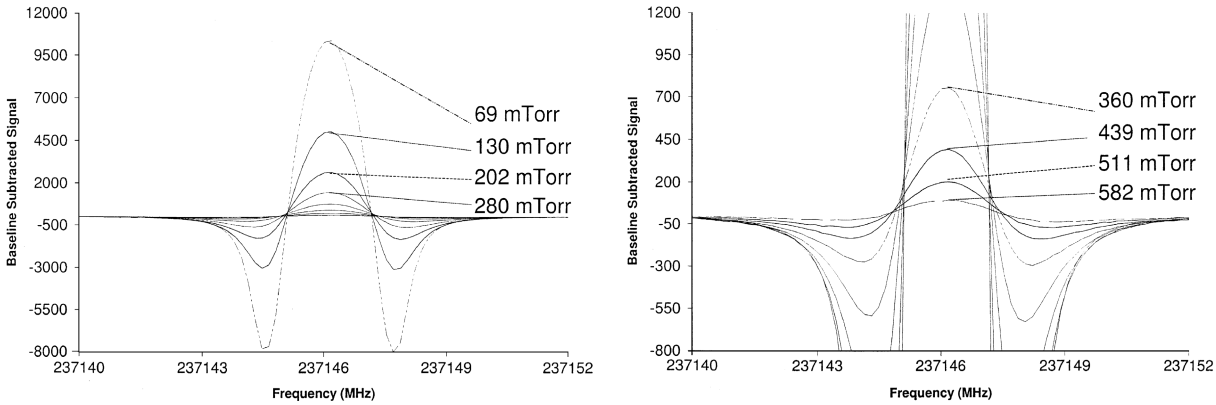

Fig. 3. The $14_{2,12} \leftarrow 14_{1,13}$ transition measured at 0.069–0.582 Torr and 220 K shown between 237140 and 237152 MHz. Graphs are depicted at full scale(left) and 10× (right).

inside the cooling jacket to minimize thermal gradients in the white cell; secondary windows were used to keep atmospheric moisture from condensing on the cold teflon surface. The total pressure is monitored with a calibrated capacitance manometer for the most accurate determination of the pressures. The pressure gauge showed deviations of less than 0.25% from actual pressure in a comparison to a standard.

3. Analysis of measurements

The O_3 rotational transitions at these temperatures and pressures consist of a lineshape that is a combination of the Doppler and the Lorentz components convolved with the instrument function. The convolution method of Pickett [12] was used to compare two scans at the same temperature and obtain a differential Lorentzian half-width, induced entirely by the increased number of foreign gas perturbers in the higher pressure scan. This method for determination of pressure broadening due to a foreign gas does not require an analytical representation of the instrumental lineshape or precise knowledge of the concentration of the absorber. An experimental spectrum $S(v, p)$ (see Fig. 3) at the pressure p is given by

$$S(v,p) = \int_{-\infty}^{\infty} S_{\mathrm{r}}(v', p') L(v - v', p - p')\,\mathrm{d}v' = S_{\mathrm{r}}(v', p') L(v - v', p - p'), \tag{1}$$

$$L(v - v', p - p') = \frac{I \Delta v_\Gamma^2}{\Delta v_\Gamma^2 + (v - v' + \Delta v_\delta)^2}, \tag{2}$$

where $S_{\mathrm{r}}(v', p')$ is a reference spectrum taken at a lower pressure p' with half-width $\Gamma(p')$ and shift $\delta(p')$. $L(v - v', p - p')$ is a Lorentzian function the half-width (Δv_Γ) and shift (Δv_δ) of which are

dependent only upon the change in pressure due to additional broadening gas. The intensity factor, I, contains the Fourier constant and scales the spectra by peak height. This Lorentzian formulation, as opposed to one scaled to peak area, provides minimal correlation between the parameters Δv_Γ and Δv_δ.

$$\Delta v_\Gamma = \Gamma(p) - \Gamma(p'), \tag{3}$$

$$\Delta v_\delta = \delta(p) - \delta(p'). \tag{4}$$

An advantage of the convolution method for lineshape analysis is that the information regarding instrumental effects, Doppler broadening, and all sources of pressure broadening common to both the low- and high-pressure samples is contained in the reference spectrum. The convolution method allows pressure broadening to be determined in the regime where there are other contributions to the lineshape. For example, if $S_r(v', p')$ is a Gaussian, $S(v, p)$ will be a Voigt profile. The requirements for the method to be valid are that the absolute pressure of the broadened molecule remain constant as the foreign gas is varied, that the absorption of the reference spectrum be linear at the line center and that the power and instrument function be constant over the broadened line profile.

The parameters of the Lorentzian are varied within a non-linear least-squares-fit to minimize the difference between the convoluted spectrum and the test spectrum. Generally, all pressures in a given run are compared for generation of a data table, N pressure measurements in a given run gives $N(N-1)/2$ data points. From eight to thirteen pressure measurements were made in any given run. At least eight runs at five different temperatures between 180 and 300 K were done for each transition in this study (56–121 data points per run, 8–13 runs per line, ~400–1000 convolution generated data points per line). Each convolution fit provides a data point consisting of differential pressure, differential half-width, differential shift and temperature for each transition. For all transitions in this study the differential shifts were found to be randomly dispersed about zero shift. Furthermore, removing this parameter from the convolutions (i.e. $\Delta v_\delta = 0$) did not change the differential half-widths. For determination of lineshape parameters the pressure broadening is assumed to have a linear pressure and power-law temperature dependence as shown in Eq. (5).

$$\Delta v_\Gamma = \gamma_o (p - p') \left(\frac{296}{T}\right)^n, \tag{5}$$

$$\Gamma(\gamma_o, n, p, T) = \gamma_o \, p \, \theta^n, \tag{6}$$

$$\begin{aligned}\Delta(\gamma_o, n, p, T) = [&(\Delta\gamma_o \, p\,\theta^n)^2 + (\Delta n \ln(\theta)\,\gamma_o \, p\,\theta^n)^2 + (\Delta p\,\gamma_o\,\theta^n)^2 \\ &+(\Delta\theta\,\gamma_o\, n\, p\theta^{n-1})^2 + 2\chi_{\gamma_o n}\Delta\gamma_o\Delta n \ln(\theta)\gamma_o p^2\theta^{2n} \\ &+2\chi_{\gamma_o p}\Delta\gamma_o\Delta p\gamma_o\, p\theta^{2n} + 2\chi_{\theta n}\Delta\theta\Delta n \ln(\theta)\,(\gamma_o p)^2 n\,\theta^{2n-1}]^{1/2},\end{aligned} \tag{7}$$

where

$$\theta = \left(\frac{296}{T}\right), \quad \Delta\theta = \left(\frac{296}{T^2}\right)\Delta T, \tag{8}$$

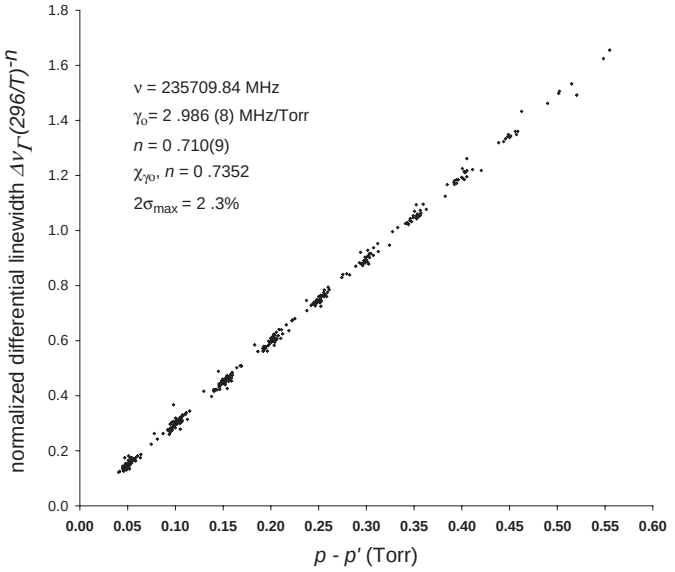

Fig. 4. Temperature normalized data set for the $16_{1,15} \leftarrow 16_{0,16}$ transition at 231281.49 MHz.

and

$$\sigma_{\max} = \Delta(\gamma_o, n, p, 180). \tag{9}$$

Values of the dependent variable $\Delta\nu_\Gamma$ are used to determine the coefficients, γ_o and n, of Eq. (5) based on a parametric fit to all temperature and differential pressure data. The parametric fit also provides the correlation coefficient between the errors of the linear pressure dependence and the exponential temperature dependence. Correlations between $\Delta\gamma_o$ and Δn, of 0.6–0.8 are typically obtained. Fig. 4 shows the complete data set for the $16_{1,15} \leftarrow 16_{0,16}$ transition when the temperature exponent $n = 0.710$ is used to normalize the pressure dependence to the reference value of 296 K. Table 2 shows the values of the parameters determined in the parametric fits. Eq. (6) allows calculation of the pure Lorenztian broadened width of a transition at arbitrary pressure and temperature. For calculation of the propagated error in the half-width (see Eq. (7)) the necessary 1σ errors (following each parameter, in units of last reported digit) and determined correlation coefficients for each transition are included in Table 2.

For calculation of random errors derived from the parameters given in Table 2, the recommended values for the pressure and temperature errors and corresponding correlation coefficients are: $\Delta p = 0.25\% p$ (Baratron calibration); $\Delta T = 1$ K (T-type thermocouple 200–350 K), $\chi_{Tn} = 1.0$ and $\chi_{\gamma_o p} = 1.0$. Note that $\chi_{pn} = 0$, $\chi_{pT} = 0$ and $\chi_{gT} = 0$ have been assumed for Eq. (7). These values give a maximum random error of 1.8–4.5% over the range of stratospheric temperatures (180–300 K) and pressures (< 100 mb). The random error typically increases 1–2.5% from 300 K down to 180 K primarily because of the increase in the relative error of the temperature measurement compounded with the larger pressure-broadened half-width at lower temperature. Maximum error values calculated at 180 K for each transition are shown in Table 2 to indicate the maximum error for the coldest stratospheric temperatures.

Table 2
Measured ozone pressure induced half-width parameters determined in this study

$J'_{K'_a,K'_c}$	J_{K_a,K_c}	$\gamma_o(296)$ (MHz/Torr)	n	$\chi_{\gamma_o n}$	$2\sigma_{\max}$[a]
$7_{1,7}$	$6_{0,6}$	3.236(8)	0.674(9)	0.7767	2.3%
$8_{3,5}$	$9_{2,8}$	3.181(17)	0.749(18)	0.8103	3.8%
$10_{2,8}$	$10_{1,9}$	3.157(6)	0.675(7)	0.7079	2.1%
$12_{0,12}$	$11_{1,11}$	3.062(10)	0.685(14)	0.7435	2.9%
$12_{2,10}$	$12_{1,11}$	3.103(7)	0.663(8)	0.6934	2.1%
$14_{1,13}$	$14_{0,14}$	2.9199			
$14_{2,12}$	$14_{1,13}$	3.037(10)	0.693(10)	0.8123	2.6%
$16_{1,15}$	$16_{0,16}$	2.986(8)	0.710(9)	0.7352	2.3%
$16_{2,14}$	$16_{1,15}$	2.971(8)	0.677(9)	0.7718	2.3%
$15_{4,12}$	$16_{3,13}$	3.014(15)	0.685(14)	0.8368	3.2%
$15_{6,10}$	$16_{5,11}$	2.988(19)[b]	0.745(25)[b]	0.6539	4.5%
$18_{1,17}$	$18_{0,18}$	3.0591	0.629		~10%
$18_{2,16}$	$18_{1,17}$	2.980(7)	0.692(8)	0.7529	2.2%
$20_{2,18}$	$20_{1,19}$	2.949(5)	0.680(5)	0.6754	1.8%
$30_{1,29}$	$30_{0,30}$	2.8615	0.543		~10%
$25_{1,25}$	$24_{0,24}$	2.7246	0.638		~10%

[a] See Eq. (9).
[b] These values calculated from measured N_2 and O_2 values using Eq. (12).

Proper application of the convolution method requires attention to a few key spectroscopic issues. Spectra should have minimal fluctuations in power and spectral dispersion as well as sufficiently weak absorption. Weak absorption was routinely checked through measurements of AM spectra indicating the maximum absorptions were 10% or less for the given partial pressure of absorber. Fluctuations in power and dispersion have been minimized through alignment and multiplier tuning to insure contributions to systematic error in the line broadening parameters are much less than 1%. Bias due to correlations between parameters have been minimized within the convolution algorithm as well as during the parametric fitting.

4. Theoretical considerations

4.1. Complex Robert–Bonamy formalism

A more complete description of the complex Robert-Bonamy (CRB) formalism [8] can be found in Refs. [17–19] here only the salient features are presented. The formalism is a semi-classical development based on the resolvent operator formalism of Baranger [20], Kolb [21], and Greim [22] (BKG) and is complex valued thus the half-width and line shift are obtained from a single calculation. The application of linked-cluster techniques [23] eliminates the awkward cutoff procedure that characterized earlier theories [24–26]. The intermolecular dynamics are correct to second-order in time utilizing curved rather than straight line trajectories based on the isotropic part of the

intermolecular potential. This has important consequences in the description of close intermolecular collisions (small impact parameters). Also important for close collision systems is the incorporation in the CRB theory of a short range (Lennard–Jones 6–12 [27]) atom–atom component to the intermolecular potential. This component has been shown to be essential for a proper description of pressure broadening, especially in systems where electrostatic interactions are weak [28]. The notion of strong and weak collisions adopts the definition of Oka [29].

The half-width, γ, and shift, δ, of a rotation band transition $f \leftarrow i$ are given in the CRB formalism by minus the imaginary part and the real part, respectively, of the diagonal elements of the complex relaxation matrix. In the mean-relative-thermal-velocity (mrtv) computational form, the half-width and line shift are usually expressed in terms of the Liouville scattering matrix ([20,30])

$$(\gamma - i\delta)_{f\leftarrow i} = \frac{n_2 \bar{v}}{2\pi c} \sum_{J_2} \langle J_2|\rho_2|J_2\rangle \int_0^\infty 2\pi b[1 - \mathrm{e}^{-S_2}]\,\mathrm{d}b, \tag{10}$$

where $\bar{v}$ is the mean relative thermal velocity, ρ_2 and n_2 are the density operator and number density of perturbers, and b is the impact parameter. S_2 is the second order term in the expansion of the Liouville scattering matrix which depends on the intermolecular potential.

The S_2 term is complex valued and anisotropic. The potential employed in the calculations consists of the leading electrostatic components for the O_3–X pair consisting of the dipole and quadrupole moments of O_3 with the quadrupole moment of N_2 or O_2, and an atom–atom component [31,17]). The atom–atom potential is defined as the sum of pair-wise Lennard–Jones 6–12 interactions [27] between atoms of the radiating molecules (labeled 1) and the perturbing molecule (labeled 2),

$$V^{at-at} = \sum_{i=1}^{n} \sum_{j=1}^{m} 4\varepsilon_{ij} \left\{ \frac{\sigma_{ij}^{12}}{r_{1i,2j}^{12}} - \frac{\sigma_{ij}^{6}}{r_{1i,2j}^{6}} \right\}. \tag{11}$$

The subscripts $1i$ and $2j$ refer to the ith atom of molecule 1 and the jth atom of molecule 2, respectively, n and m are the number of atoms in molecules 1 and 2, respectively, and ε_{ij} and σ_{ij} are the Lennard–Jones parameters for the atomic pairs. The heteronuclear atom–atom parameters can be constructed from homonuclear atom–atom parameters (ε_i and σ_i) by the combination rules of Hirschfelder et al. [32] or Good and Hope [33].

The atom–atom distance, r_{ij} is expressed in terms of the center of mass separation, R, via the expansion of Sack [34]. The expansion in $(1/R)$ must be truncated, sufficient order must be chosen to insure the convergence of calculated half-widths and line shifts. The order of the expansion has been discussed by Labani et al. [35] and by Gamache et al. [31,17,18]. Here the formulation of Neshyba and Gamache [31] expanded to eighth order is used.

The isotropic component of the atom–atom potential is used to define the trajectory of the collision within the semiclassical model of Robert and Bonamy [8]. The temperature dependence of the half-width was taken as its usual form [36,37] as discussed earlier for the laboratory measurements (see Eq. (6)). The reference temperature, $T_0 = 296$ K, is not restricted to this value but is the usual choice.

Eq. (6) is approximate. Simplified models for the temperature dependence of the half-width have been discussed by Birnbaum [38] or Bonamy et al. [39]. The methods are based on the temperature

Table 3
Molecular moments used in the CRB calculations

Molecule	Multipole moment (esu)	Ref.
O_3	$m = 0.532 \times 10^{-18}$	[44]
	$Q_{xx} = -1.40 \times 10^{-26}$	[44]
	$Q_{yy} = -0.70 \times 10^{-26}$	[44]
	$Q_{zz} = 2.10 \times 10^{-26}$	[44]
N_2	$Q_{zz} = -1.4 \times 10^{-26}$	[45]
O_2	$Q_{zz} = -0.4 \times 10^{-26}$	[46]

dependence of the terms in the intermolecular potential. Unfortunately, the intermolecular potentials that mimic the true interaction generally contain too many terms for the analysis of Refs. [38] and [39]. The intermolecular potential employed in the calculations presented here contains 170 terms. However, the general forms of the dependencies can still be of value.

Better models have been proposed for the temperature dependence of the half-width. Pack [40], in a study of CO_2 broadened by He and Ar, proposed a polynomial in T for the temperature dependence of the half-width; $\gamma = c_1 T^{-1} + c_2 + c_3 T^1$. More recently in a study of the temperature dependence of the half-width of the 500.4 GHz transition ($34_{2,32} \leftarrow 34_{1,33}$) of the ground vibrational state of ozone Gamache [41], at the suggestion of Rossi [42], proposed a double power law model; $\gamma(T) = b_0\{T_0/T\}^{b_1} + b_2\{T_0/T\}^{b_3}$, which correctly modeled the temperature dependence when the temperature range was large. For the temperature range considered in this paper, Eq. (6) is an appropriate model.

4.2. Theoretical calculations

Calculations of the half-width and line shift based on the CRB formalism were made for the 22 pure rotational transitions of O_3 listed in Table 1 at 150, 225, 296, 350 and 450 K with N_2 and O_2 as the perturbing gases. The CRB formalism yields the half-width and line shift from a single calculation and there are no adjustable parameters or cutoff procedure [43] in the formalism.

All molecular parameters used in this work are the best available values from the literature. No molecular constants have been adjusted to give better agreement with experiment. The dipole and quadrupole moments of ozone are taken from Ref. [44]. The quadrupole moment of nitrogen is from Mulder et al. [45] and that for oxygen is from Stogryn and Stogryn [46]. The numerical values are listed in Table 3. The atom–atom parameters were obtained using the standard combination rules [32] with the atom–atom parameters for homonuclear diatomics determined by Bouanich [47] by fitting to second virial coefficient data. These parameters are reported in Table 4. The atom–atom potential is expanded to eighth-order in the molecular centers of mass separation. In the parabolic trajectory approximation the isotropic part of the interaction potential is taken into account in determining the distance, effective velocity, and force at closest approach [8]. To simplify the trajectory calculations the isotropic part of the atom–atom expansion is fit to an isotropic Lennard–Jones 6–12 potential, giving $\varepsilon/k = 43.9$ K and $\sigma = 3.15$ Å for the ozone–nitrogen collision pair and $\varepsilon/k = 51.73$ K and $\sigma = 3.01$ Å for the ozone–oxygen collision pair.

Table 4
Values of the heteronuclear atom–atom parameters for the collision pairs

Atomic pair	σ (Å)	$\varepsilon/k_B(K)$
O–N	3.148	43.90
O–O	3.010	51.73

Table 5
CRB calculated half-widths and line shifts at 296 K in units of MHz/Torr for N_2-, O_2-, and air-broadening of ozone transitions in the rotation band

$J'_{K'_aK'_c}$	J_{K_a,K_c}	$\gamma_o(N_2)$	$\delta_o(N_2)$	$\gamma_o(O_2)$	$\delta_o(O_2)$	γ_o(air)	δ_o(air)
$15_{6,10}$	$16_{5,11}$	3.099	−0.004	2.680	−0.006	3.011	−0.004
$37_{9,29}$	$36_{8,28}$	2.768	0.004	2.293	0.001	2.668	0.003
$31_{10,22}$	$30_{9,21}$	2.828	0.009	2.369	0.000	2.732	0.007
$24_{5,19}$	$25_{4,22}$	2.842	0.002	2.360	0.005	2.741	0.003
$16_{1,15}$	$16_{0,16}$	3.053	0.005	2.470	0.010	2.931	0.006
$16_{2,14}$	$16_{1,15}$	3.021	−0.001	2.472	0.001	2.906	−0.001
$14_{2,12}$	$14_{1,13}$	3.091	−0.001	2.565	−0.001	2.981	−0.001
$18_{2,16}$	$18_{1,17}$	2.966	−0.001	2.403	0.003	2.848	0.000
$12_{2,10}$	$12_{1,11}$	3.165	0.000	2.666	−0.002	3.060	0.000
$12_{0,12}$	$11_{1,11}$	3.210	0.006	2.664	0.010	3.095	0.007
$15_{4,12}$	$16_{3,13}$	3.049	0.000	2.572	−0.006	2.949	−0.001
$20_{2,18}$	$20_{1,19}$	2.924	−0.002	2.357	0.003	2.805	−0.001
$7_{1,7}$	$6_{0,6}$	3.299	−0.005	2.838	0.001	3.202	−0.004
$8_{3,5}$	$9_{2,8}$	3.296	0.008	2.873	−0.004	3.207	0.005
$10_{2,8}$	$10_{1,9}$	3.234	0.001	2.766	0.000	3.136	0.001
$14_{1,13}$	$14_{0,14}$	3.115	0.005	2.555	0.011	2.997	0.006
$5_{1,5}$	$4_{0,4}$	3.312	−0.009	2.874	0.001	3.220	−0.007
$18_{1,17}$	$18_{0,18}$	3.001	0.008	2.406	0.014	2.876	0.009
$9_{1,9}$	$8_{0,8}$	3.275	−0.002	2.783	0.004	3.172	−0.001
$28_{1,27}$	$28_{0,28}$	2.845	0.010	2.304	0.005	2.731	0.009
$30_{1,29}$	$30_{0,30}$	2.824	0.009	2.299	−0.006	2.714	0.006
$25_{1,25}$	$24_{0,24}$	2.875	−0.007	2.309	−0.011	2.756	−0.008

To evaluate the reduced matrix elements rotational–vibrational wave functions are needed. The ground vibrational state wavefunctions used in the calculations are determined with the Watson–Hamiltonian constants of Camy–Peyret and Flaud [48]. The molecular constants for N_2 and O_2 are from Huber and Herzberg [49].

Using Eq. (6) with the temperatures and corresponding calculated half-widths a least-squares fit can be made to determine the temperature exponent, n, and the correlation coefficient of the fit. The uncertainty of the calculated temperature exponents is determined for each transition by the following procedure. Values of n are determined using any two of the five calculated points. This generates ten 2-points values of n. The uncertainty assigned to the calculation is the maximum difference between the least-squares fit value and the ten 2-points values.

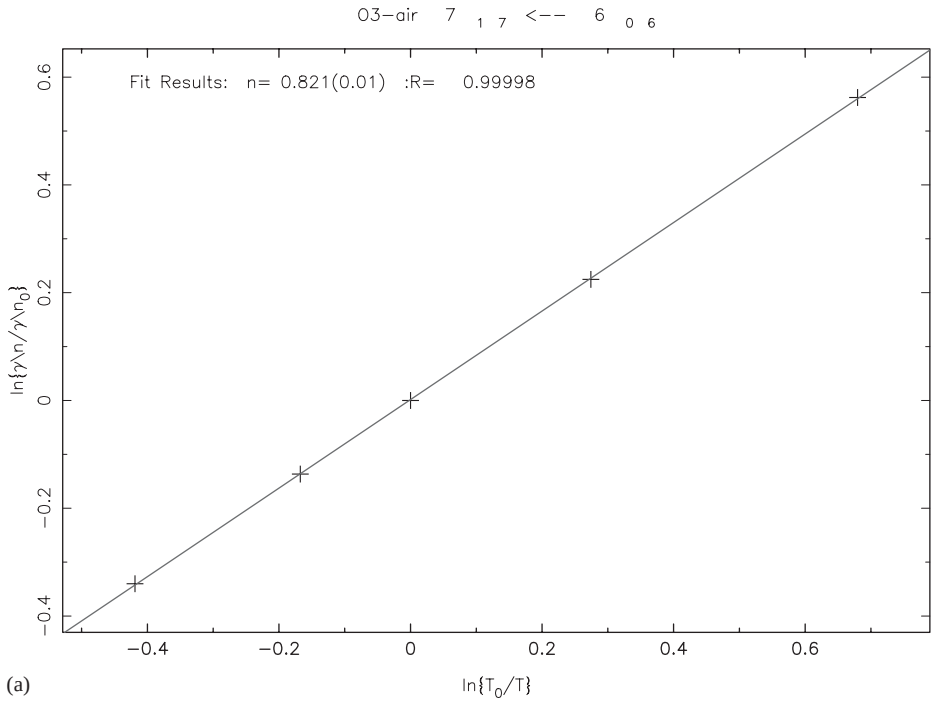

(a)

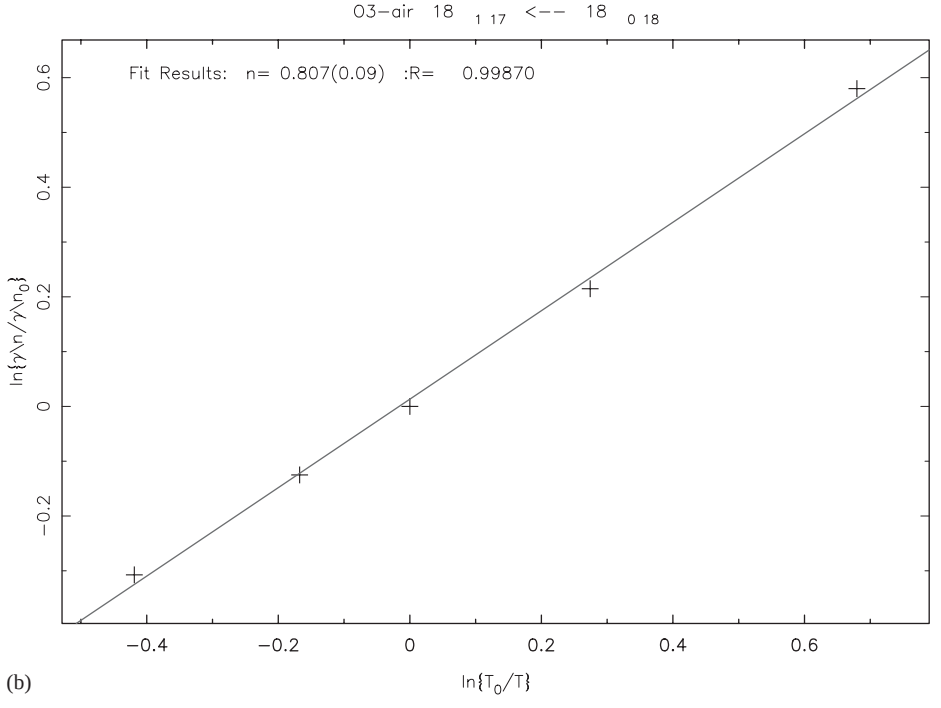

(b)

Fig. 5. Theoretical calculations of the temperature dependence of the pressure-induced half-width exhibiting (a) normal power-law behavior for the $7_{1,7} \leftarrow 6_{0,6}$ transition and (b) deviations from the power-law expression for the $18_{1,17} \leftarrow 18_{0,18}$ transition of O_3.

Table 6
Temperature dependence of the air-broadened half-width of ozone transitions in the rotation band with the estimated error in parenthesis, correlation coefficient, R, of the fits, and reduced temperature range fit

$J'_{K'_a,K'_c}$	J_{K_a,K_c}	n (150–450 K)	R	n (225–350 K)
$5_{1,5}$	$4_{0,4}$	0.830(14)	0.99997	0.823
$7_{1,7}$	$6_{0,6}$	0.820(12)	0.99998	0.82
$8_{3,5}$	$9_{2,8}$	0.790(13)	0.99998	0.78
$9_{1,9}$	$8_{0,8}$	0.810(13)	0.99998	0.806
$10_{2,8}$	$10_{1,9}$	0.790(20)	0.99995	0.78
$12_{2,10}$	$12_{1,11}$	0.780(35)	0.99983	0.77
$12_{0,12}$	$11_{1,11}$	0.800(39)	0.99981	0.78
$14_{1,13}$	$14_{0,14}$	0.790(64)	0.99943	0.76
$14_{2,12}$	$14_{1,13}$	0.780(55)	0.99955	0.76
$16_{1,15}$	$16_{0,16}$	0.790(72)	0.99923	0.76
$16_{2,14}$	$16_{1,15}$	0.790(76)	0.99912	0.76
$15_{4,12}$	$16_{3,13}$	0.790(71)	0.99924	0.76
$15_{6,10}$	$16_{5,11}$	0.790(55)	0.99954	0.77
$18_{2,16}$	$18_{1,17}$	0.800(86)	0.99881	0.77
$18_{1,17}$	$18_{0,18}$	0.810(94)	0.99870	0.770
$20_{2,18}$	$20_{1,19}$	0.820(92)	0.99876	0.79
$25_{1,25}$	$24_{0,24}$	0.820(92)	0.99877	0.790
$24_{5,19}$	$25_{4,22}$	0.830(96)	0.99875	0.80
$28_{1,27}$	$28_{0,28}$	0.840(89)	0.99889	0.808
$30_{1,29}$	$30_{0,30}$	0.830(86)	0.99893	0.806
$31_{10,22}$	$30_{9,21}$	0.810(72)	0.99922	0.79
$37_{9,29}$	$36_{8,28}$	0.820(73)	0.99920	0.79

4.3. Theoretical results

The air-broadened half-widths for the 22 transitions studied were determined from the N_2- and O_2-broadened half-widths using Eq. (12). The calculated N_2-, O_2-, and air-broadened half-width and line shift are given in Table 5.

$$\gamma_{\text{air}} = 0.79\gamma_{N_2} + 0.21\gamma_{O_2}. \tag{12}$$

The temperature dependence parameters, n, of the air-broadened half-widths given by Eq. (6) are given in Table 6 with the estimated error and the correlation coefficient of the fit. Fig. 5 shows plots of $\ln[\gamma(T)/\gamma(T_0)]$ versus $\ln[T_0/T]$ for air-broadening of the $7_{1,7} \leftarrow 6_{0,6}$ and $18_{1,17} \leftarrow 18_{0,18}$ transitions of O_3. The first of these figures is an example for which the model (Eq. (6)) is a good approximation to the temperature dependence of the half-width. The correlation coefficient for the fit of this line is 0.99997. However, for the second figure ($18_{1,17} \leftarrow 18_{0,18}$ transition) the fit over the temperature range 150–450 K is not correctly modeled by Eq. (6), with a correlation coefficient of 0.99870. As discussed by Gamache [41] when the temperature range is large, expression 6 does not fit the data accurately and a more complex model is needed. The measured temperature exponents were from a fit of the range 180–300 K. The last column of Table 6 gives the temperature

exponent determined from the CRB calculations over the range 225–350 K. The change in temperature range yields temperature exponents that are on average 3% lower with a maximum lowering of ~5%. The temperature exponents determined from the reduced temperature range are in better agreement with the measured values. There is also the question of the difference between mean-relative-thermal-velocity (mrtv) calculations versus calculations made including the average over the relative velocity [41]. In the study of Ref. [41] the difference between the two methods of calculation was ~5% for the temperature dependence of the half-width.

5. Discussion

5.1. Sources of error

The possible experimental sources of error have been minimized. However, the assumption that the gas flowing through the spectrometer has reached thermal equilibrium with the cell is considered as a potential source of systematic error in the temperature measurement. Another potential source for systematic error is the assumption that the absorber partial pressure is constant throughout an experimental run. These possibilities and the influence on the reported parameters will now be discussed.

As mentioned previously, the convolution method requires the absorber partial pressure to remain constant for reliable results. Experimentally, the O_3 partial pressure was often variable. Ideally, the partial pressure was kept to ~ 1 mTorr, but weaker transitions often required up to 15 mTorr O_3 for sufficient S/N. In runs where the partial pressure was > 10 mTorr a significant *decrease* in the O_3 partial pressure could be observed as the buffer gas pressure was *increased*. For an O_3 self-broadened half-width *larger* than the air-broadened half-width the decrease in partial pressure of O_3 (and subsequent overestimate of buffer gas pressure) would cause an apparent *decrease* in the half-width determined for the data run. For each data point in concern the O_3 self-broadened half-width was measured under the same conditions for estimation of the systematic error introduced by the partial pressure changes. The values for ozone self-broadened half-width fall into the range, $\gamma_o(296) = 4.04$–4.71 MHz/Torr and $n = 0.74$–1.24, with the average values, $\gamma_o(296) = 4.44$ MHz/Torr and $n = 0.98$. Using the individual O_3 self-broadened half-width parameters and partial pressure deviations the *narrowed* half-width for a suspect run was checked *vs.* the *normal* value. Normally the value did not change more than 0.5%, a surprising result that rectifies the use of *all* $N(N-1)$ values available in a comparison of N scans. When the values were more than 1% different, the run was not used in the parametric fit.

Temperature gradients within the flow of the gas due to slow equilibration and/or contact with warmer windows would increase as the bath temperature is moved further from room temperature, therefore increasing the error of the temperature measurement proportionately to the difference between the cell temperature and room temperature. Furthermore, the directionality of this potential systematic error source would always cause n to be underestimated. Such an error would scale to the cell dimensions, and if large enough to be a problem, would be noticeable with the use of a variety of different length and/or diameter cells. For the 625.4 GHz ($15_{6,10} \leftarrow 16_{5,11}$) transition in this study, two different cells ($L = 0.5$ and 1.0 m) were used during experimentation and measurements overlapped within the uncertainties, in fact the shorter cell showed a slightly larger temperature

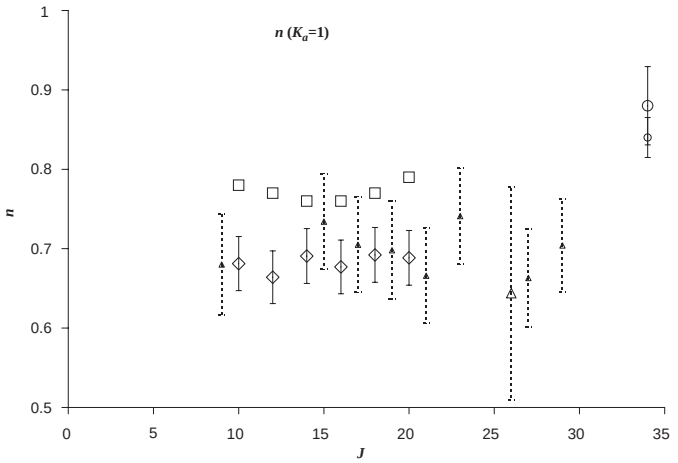

Fig. 6. Comparisons of measured and calculated values for the temperature dependence of the pressure induced half-width for the various $K_a = 1$ transitions. ◇—Measured rotational (this study), ◯—measured rotational (CNRS) [15], △—measured vibrational v_1 branch (Langley) [14] and □—calculated rotational (this study).

exponent. If such a systematic error exists it must be significantly smaller than the random error. Furthermore, the magnitudes of the measured exponents are consistent with comparisons to other temperature dependent studies such as Smith [14] where very similar values are determined for the $K_a = 1$ transitions (see Fig. 6).

Theoretical values for the temperature exponents are all higher than measured values, with the values coming into closer agreement when the calculated values are limited to a similar temperature range compared to the measured values. Ideally, the pressure and temperature dependencies determined by theory and experiment would randomly disperse. The theoretical values are all larger as the temperature decreases as shown in the analogous plot for the exponents. Interestingly, the crossing point is at higher temperatures for the two largest J transitions.

5.2. Comparisons of results

Measurements have been reported for O_3 in the 240 and 640 GHz bands of EOS-MLS, and calculations for transitions for these as well as the transitions located in 2.5 THz band. Experimental measurements of these transitions are planned using a different spectrometer. In addition to the fourteen transitions of interest to EOS-MLS, eight additional transitions were investigated to provide further comparison of the present work to existing infrared and previous FIR and mm-wave results.

Plots of the J-dependence of the half-width are shown in Fig. 7 for the $J_{2,J-2} \leftarrow J_{1,J-1}$ and $J_{1,J-1} \leftarrow J_{0,J}$ Q branches that are predominant features in the rotational bands. The agreement between the present experiments and CRB calculations is quite good at $J < 15$ for the Q branch and at all comparable values for $K_a = 0$. The monotonic decrease in half-width with increase in J is readily extended to show agreement with measurements of Smith et al. [14] for the v_1 branch and the single measurement in the submillimeter by Priem et al. [15].

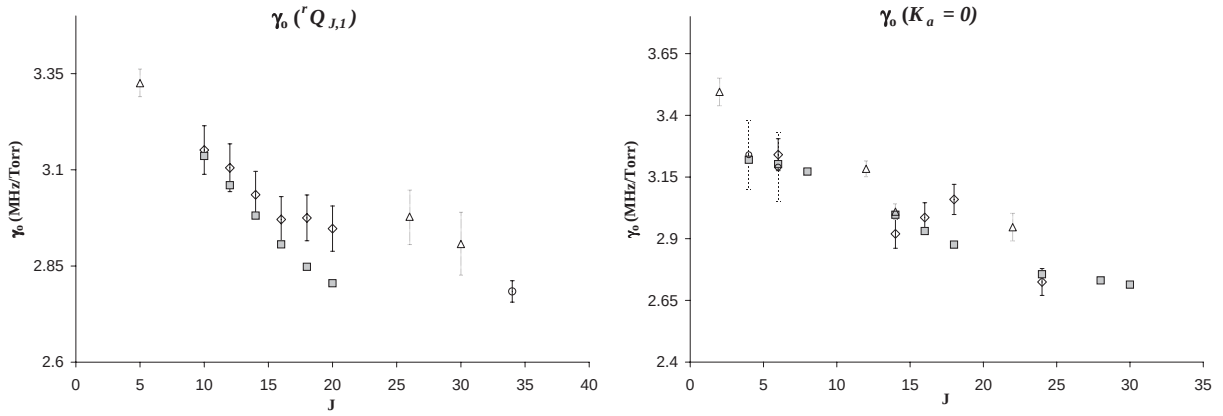

Fig. 7. Comparisons of measured and calculated values for pressure induced half-width values at 296 K for the $J_{2,J-2} \leftarrow J_{1,J-1}$ transitions (left) and various $K_a = 0$ transitions (right). ◇—Measured rotational (this study), ◯—measured rotational (CNRS) [15] (left) Connor [50] (right), △—measured vibrational v_1 branch (Langley) [14] and □—calculated rotational (this study).

Comparisons to other branches in the v_1 data [14] show very good agreement among similar J, K_a transitions. Unlike the Q branches, the R branches reported in Ref. [14] are for many of the same J values as measured for Q branches in this work. Not shown in Fig. 7 is the $J+1_{2,J} \leftarrow J_{1,J-1}$ and $J+1_{1,J} \leftarrow J_{0,J}$ R type branches reported by Smith et al. these values all overlap the measurements of this study. As theory has suggested, there seems to be very little vibrational dependence of the half-width parameters.

The FIR study of Larsen [16] reports an extensive number of half-widths for higher values of K_a. A few of the transitions in the present work can be compared by extrapolation of the J-dependence to lower values. Comparison of the $15_{6,10} \leftarrow 16_{5,11}$ branch transition to similar K_a values in [16] shows an agreeable trend of increasing half-width for decreasing J, as observed for the lower values of K_a.

The absence of measurable shifts in the rotational spectra is not unexpected since the theoretical results give a maximum δ_o of 0.009 MHz/Torr. Line shifts in air have been measured in the v_1 band that range from -0.288 to 0.180 MHz/Torr. This result is expected since the theory has shown that the dominant part of the intermolecular potential responsible for the line shift is the vibrational dephasing term, S_1. Whenever there is a change in vibrational state for the transition the S_1 term is non zero and tends to be greater than the imaginary parts of the S_2 terms. The contribution of the S_1 term is independent of the rotational states. As the number of vibrational quanta exchanged in a transition increases the S_1 contribution increases and the line is approximately given by the S_1 contribution plus small fluctuations about this value given by the rotational contributions to the shift.

Comparisons of the temperature exponent, n, show a generic agreement throughout experiments, with values typically falling in the range 0.6–0.8 without any obvious J, K_a dependence. The CRB results do not show nearly as much randomness and are often larger than the measured values. Any trends suggested by the CRB calculations cannot be verified due to the present accuracy limits in the measured values.

6. Conclusion

This paper has presented a comprehensive analysis of the air-broadened O_3 millimeter and submillimeter rotational transitions that will facilitate the study of O_3 in the Earth's stratosphere and upper troposphere. The work produces several broadening parameters precise to 2% at the 2σ level, and indicates clear trends in the J and K_a dependence of the half-width parameters in showing agreement between rotational, vibrational and theoretical studies.

Acknowledgements

This paper presents research carried out at the Jet Propulsion Laboratory, California Institute of Technology, under contract with the National Aeronautics and Space Administration. The authors (RRG and JF) are pleased to acknowledge support of this research by the National Science Foundation through Grant No. ATM-9812540. Any opinions, findings, and conclusions or recommendations expressed in this material are those of the author(s) and do not necessarily reflect the views of the National Science Foundation or NASA.

References

[1] Waters JW, Read WG, Froidevaux L, Jarnot RF, Cofield RE, Flower DA, Lau GK, Pickett HM, Santee ML, Wu DL, Boyles MA, Burke JR, Lay RR, Loo MS, Livesey NJ, Lungu TA, Manney GL, Nakamura LL, Perun VS, Ridenoure BP, Shippony Z, Siegel PH, Thurstans RP, Harwood RS, Pumphrey HC, Filipiak MJ. The UARS and EOS microwave limb sounder (MLS) experiments. J Atmos Sci 1999;56:194.

[2] Pardo JR, Pagani L, Olofsson G, Febvre P, Tauber J. Balloon-borne submillimeter observations of upper stratospheric O_2 and O_3. JQSRT 2000;67:169–80.

[3] deValk JPJMM, Goede APH, deJonge ARW, Mees J, Franke B, Crewell S, Kullmann H, Urban J, Wohlgemuth J, Chipperfield MP, Lee AM. Airborne heterodyne measurements of stratospheric ClO, HCl, O_3, and N_2O during SESAME 1 over northern Europe. J Geophys Res—Atmospheres 1997;102:1391–8.

[4] Carli B, Ade P, Carlotti M, Cortesi U, Gignoli A, Hamilton P, Lanfranchi M, Lee C, MacKenzie AR, Phillips A. Minor constituent concentrations measured from a high altitude aircraft using high resolution far-infrared Fourier Transform spectroscopy. J Atmos Chem 2000;35:273–93.

[5] Chance K, Traub WA, Johnson DG, Jucks KW, Ciarpallini P, Stachnik RA, Salawitch RJ, Michelsen HA. Simultaneous measurements of stratospheric HO_x, NO_x, and Cl_x: comparison with a photochemical model. J Geophys Res—Atmospheres 1996;101:9031–43.

[6] Pickett HM, Poynter RL, Cohen EA, Delitsky ML, Pearson JC, Müller HSP. Submillimeter, millimeter, and microwave spectral line catalog. JQSRT 1998;60(5):883–90. See also http://spec.jpl.nasa.gov/.

[7] Rothman LS, Rinsland CP, Goldman A, Massie ST, Edwards DP, Flaud JM, Perrin A, Camy-Peyret C, Dana V, Mandin JY, Schroeder J, McCann A, Gamache RR, Wattson RB, Yoshino K, Chance KV, Jucks KW, Brown LR, Nemtchinov V, Varanasi P. The HITRAN Molecular Spectroscopic Database and HAWKS (HITRAN Atmospheric Workstation): 1996 Edition. JQSRT 1998;60:665. See also http://cfa-www.harvard.edu/HITRAN/.

[8] Robert D, Bonamy J. Short-range force effects in semi-classical molecular line broadening calculations. J Phys (Paris) 1979;40:923.

[9] Gamache RR. Analytical evaluation of the Maxwell–Boltzmann velocity average in pressure-broadened half-width calculations. J Mol Spec 2001;208:79.

[10] Gamache RR, Arié E, Boursier C, Hartmann JM. Pressure-broadening and pressure-shifting of spectral lines of ozone. Spectrochim Acta A 1998;54:35–63.

[11] Oswald JE, Koch T, Mehdi I, Pease A, Dengler RJ, Lee TH, Humphrey DA, Kim M, Siegel PH, Frerking MA, Erickson NR. Planar diode solid-state receiver for 557 GHz with state-of-the-art performance. IEEE Microwave Guided Wave Lett 1998;8:232.
[12] Pickett HM. Determination of collisional linewidths and shifts by a convolution method. Appl Opt 1980;19:2745.
[13] Oh JJ, Cohen EA. Pressure broadening of ozone lines near 184 and 206 GHz by nitrogen and oxygen. JQSRT 48;405–8.
[14] Smith MAH, Devi VM, Benner DC, Rinsland CP. Temperature dependence of air-broadening and shift coefficients of O_3 lines in the ν_1 band. J Mol Spec 1997;182:239.
[15] Priem D, Colmont JM, Rohart F, Wlodarczak G, Gamache RR. Relaxation and lineshape of the 500.4-GHz line of ozone perturbed by N_2 and O_2. J Mol Spec 2000;204:204–22.
[16] Larsen RW, Nicolaisen FM, Sørensen GO. Determination of self-, air-, and oxygen-broadening coefficients of pure rotational absorption lines of ozone and of their temperature dependencies. J Mol Spec 2001;210:259.
[17] Gamache RR, Lynch R, Neshyba SP. New developments in the theory of pressure-broadening and pressure-shifting of spectral lines of H_2O: the complex Robert-Bonamy formalism. JQSRT 1998;59:319–35.
[18] Lynch R, Gamache RR, Neshyba SP. N_2 and O_2 induced halfwidths and line shifts of water vapor transitions in the $(301) \leftarrow (000)$ and $(221) \leftarrow (000)$ bands. JQSRT 1998;59:595–613.
[19] Lynch R. Ph.D. dissertation, Physics Department, University of Massachusetts Lowell, June 1995.
[20] Baranger M. General impact theory of pressure broadening. Phys Rev 1958;112:855–65.
[21] Kolb AC, Griem HR. Theory of line broadening in multiplet spectra. Phys Rev 1958;111:514–21.
[22] Griem H. Plasma Spectroscopy. New York: McGraw-Hill, 1964.
[23] Kubo R. Generalized cumulant expansion method. J Phys Soc Japan 1962;17:1100–20.
[24] Anderson PW. Dissertation, Harvard University, 1949.
[25] Anderson PW. Pressure broadening in the microwave and infra-red regions. Phys Rev 1949;76:647–61; Anderson PW. Pressure broadening in the microwave and infra-red regions. Phys Rev 1950;80:511–3.
[26] Tsao CJ, Curnutte Jr B. Linewidths of pressure-broadened spectral lines. JQSRT 1962;2:41–91.
[27] Lennard-Jones JE. Proc Roy Soc 1924;A106:463–77.
[28] Neshyba SP, Lynch R, Gamache R, Gabard T, Champion JP. Pressure-induced widths and shifts for the ν_3 band of methane. J Chem Phys 1994;101:9412–21.
[29] Oka T. In: Bates DR, editor. Advances in Atomic and Molecular Physics. New York: Academic Press, 1973.
[30] Ben-Reuven A. In: Prigogine I, Rice SA, editors. Spectral line shapes in gases in the binary-collision approximation. Adv Chem Phys, Vol. 20. New York: Academic Press, 1975. p. 235.
[31] Neshyba SP, Gamache RR. Improved line-broadening coefficients for asymmetric rotor molecules with application to ozone lines broadened by nitrogen. JQSRT 1993;50:443–53.
[32] Hirschfelder JO, Curtiss CF, Bird RB. Molecular theory of gases and liquids. New York: Wiley, 1964.
[33] Good RJ, Hope CJ. Test of combining rules for intermolecular distances, potential function constants from second virial coefficients. J Chem Phys 1971;55:111–6.
[34] Sack RA. 2-Center expansion for powers of distance between 2 points. J Math Phys 1964;5:260.
[35] Labani B, Bonamy J, Robert D, Hartmann JM, Taine J. Collisional broadening of rotation-vibration lines for asymmetric-top molecules. 1. Theoretical-model for both distant and close collisions. J Chem Phys 1986;84: 4256–67.
[36] Gamache RR. Temperature-dependence of N_2-broadened halfwidths of ozone. J Mol Spectrosc 1985;114:31–41.
[37] Gamache RR, Rothman LS. Temperature-dependence of N_2-broadened halfwidths of water-vapor—The pure rotation and ν_2 bands. J Mol Spectrosc 1988;128:360–9.
[38] Birnbaum G. In: Hirschfelder JO, editor. Intermolecular Forces. New York: Interscience, 1967. p. 487.
[39] Bonamy J, Robert D, Boulet C. Simplified models for the temperature-dependence of linewidths at elevated temperatures and applications to CO broadened by Ar and N_2. JQSRT 1984;31:23–34.
[40] Pack RT. Pressure broadening of the dipole and Raman lines of CO_2 by H_2 and Ar, temperature dependence. J Chem Phys 1979;70:3424–33.
[41] Gamache RR. Analytical evaluation of the Maxwell–Boltzmann velocity average in pressure-broadened half-width calculations. J Mol Spectrosc 2001;208:79–86.
[42] Rossi L. Department of Mathematical Sciences, University of Massachusetts Lowell, Private communication, 2000.

[43] Tipping RH, Herman RM. Impact theory for noble gas pressure-induced HCl vibration-rotation and pure rotation line width. Part 1. JQSRT 1970;10:881;
Tipping RH, Herman RM. Impact theory for noble gas pressure-induced HCl vibration-rotation and pure rotation line shifts. Part 2. JQSRT 1970;10:897.
[44] Mack KM, Muenter JS. Stark and Zeeman properties of ozone from molecular-beam spectroscopy. J Chem Phys 1977;66:5278.
[45] Mulder F, Van Dijk G, Van der Avoird A. Multipole moments, polarizabilities and anisotropic long-range interaction coefficients for N_2. Mol Phys 1980;39:407.
[46] Stogryn DE, Stogryn AP. Molecular multipole moments. Mol Phys 1966;11:371.
[47] Bouanich JP. Site Lennard-Jones potential parameters for N_2, O_2, H_2, CO and CO_2. JQSRT 1992;47:243.
[48] Flaud JM, Camy-Peyret C. Private communication, Université Pierre et Marie Curie, Paris, France, 1994.
[49] Huber KP, Herzberg G. Molecular Spectra and Molecular Structure: Constants of Diatomic Molecules. New York: Van Nostrand, 1979.
[50] Connor BJ, Radford HE. Pressure broadening of millimeter-wave ozone lines by atmospheric gases. J Mol Spec 1986;117:15.